Published in final edited form as:

Clin Cancer Res. 2022 July 01; 28(13): 2953–2968. doi:10.1158/1078-0432.CCR-21-3039.

Stress Keratin 17 expression in head and neck cancer contributes to immune evasion and resistance to immune checkpoint blockade

Wei Wang[1], **Taja Lozar**[1,2], **Athena E. Golfinos**[1], **Denis Lee**[1], **Ellery Gronski**[1], **Ella Ward-Shaw**[1], **Mitchell Hayes**[1], **Justine Y. Bruce**[3], **Randall J Kimple**[4], **Rong Hu**[5], **Paul M. Harari**[4], **Jin Xu**[5], **Aysenur Keske**[5], **Paul M. Sondel**[4,6], **Megan B. Fitzpatrick**[5], **Huy Q. Dinh**[1,6,7], **Paul F. Lambert**[1,6]

[1]McArdle Laboratory for Cancer Research/ Department of Oncology, University of Wisconsin School of Medicine and Public Health, Madison WI, USA

[2]University of Ljubljana, Ljubljana, Slovenia

[3]Department of Medicine, University of Wisconsin School of Medicine and Public Health, Madison, Wisconsin, USA

[4]Department of Human Oncology, University of Wisconsin School of Medicine and Public Health, Madison WI, USA

[5]Department of Pathology and Laboratory Medicine, University of Wisconsin School of Medicine and Public Health, Madison, Wisconsin, USA

[6]University of Wisconsin Carbone Cancer Center, University of Wisconsin School of Medicine and Public Health, Madison

[7]Department of Biostatistics and Medical Informatics, University of Wisconsin School of Medicine and Public Health, Madison WI, USA

Abstract

Purpose: We investigated whether in human head and neck squamous cell carcinoma (HNSCCs), high levels of expression of stress keratin 17 (K17), is associated with poor survival and resistance to immunotherapy.

Experimental Design: We investigated the role of K17 in regulating both the tumor microenvironment and immune responsiveness of HNSCC using a syngeneic mouse HNSCC model, MOC2. MOC2 gives rise to immunologically cold tumors that are resistant to immune checkpoint blockade (ICB). We engineered multiple, independent K17 knockout (KO) MOC2 cell lines and monitored their growth and response to ICB. We also measured K17 expression in human HNSCC of patients undergoing ICB.

Corresponding authors: Huy Q, Dinh, 7553 Wisconsin Institute Medical Research, 1111 Highland Ave, Madison, WI, 53705, USA, huy.dinh@wisc.edu, tel.: (608) 263-2890; Paul F. Lambert, 6459 Wiscomnsin Institute Medical Research, 1111 Highland Ave., Madison, WI, 53705, USA, plambert@wisc.edu, tel.: (608) 262-8533.

The authors declare no potential conflicts of interest.

Results: MOC2 tumors were found to express K17 at high levels. When knocked out for K17 (K17KOMOC2), these cells formed tumors that grew slowly or spontaneously regressed and had a high CD8+ T cell infiltrate in immunocompetent syngeneic C57/BL6 mice compared to parental MOC2 tumors. This phenotype was reversed when we depleted mice for T cells. Whereas parental MOC2 tumors were resistant to ICB treatment, K17KO MOC2 tumors that didn't spontaneously regress were eliminated upon ICB treatment. In a cohort of HNSCC patients receiving Pembrolizumab, high K17 expression correlated with poor response. Single cell RNA seq analysis revealed broad differences in the immune landscape of K17KO MOC2 tumors compared to parental MOC2 tumors, including differences in multiple lymphoid and myeloid cell types.

Conclusions: We demonstrate that K17 expression in HNSCC contributes to immune evasion and resistance to immune checkpoint blockade treatment by broadly altering immune landscapes of tumors.

Translational relevance

The response rate of head and neck cancer to immune checkpoint blockade (ICB) therapies is around 25%. Low response rate to ICB often results from the immunologically cold status of tumor microenvironment. This study identifies the overexpression of stress keratin 17 as a mechanism by which head and neck cancer evades immune response and resists to ICB therapies. Both HPV+ and HPV- human head and neck cancer can have overexpression of stress keratin 17, which correlates with shorter overall survival. Utilizing an immunologically cold, syngeneic, mouse tumor model, we demonstrate that stress keratin 17 expression in tumors correlates with immunological cold tumor microenvironment and resistance to ICB treatment *in vivo*, partially through inhibiting CXCR3-mediated chemotaxis. These findings provide a foundation for future studies to identify novel targets to improve immunotherapy efficacy, and to further evaluate stress keratin 17 as a predictive marker for response to immunotherapy.

Introduction

Stress keratin 17 (K17) is a stress-induced keratin expressed in epithelial cells during wound healing, inflammation and autoimmune diseases (1–4). In normal healthy epithelium, expression of K17 is limited to the medulla compartment of the hair and skin appendages (4, 5). K17 is overexpressed in a variety of cancer types, including cancers of the skin, cervix, breast, ovary and the head and neck region, and is associated with poor prognosis in breast, oropharyngeal and ovarian cancers (6–11). How K17 contributes to a worse prognosis in cancer patients is unclear. Disruption of the K17 gene in Human Papillomavirus (HPV) transgenic mice and in Gli2 transgenic mice suppressed cervical and skin carcinogenesis, respectively, and led to a differential cytokine expression profile suggesting a role of K17 in host immunity (6, 12). Our prior work using mouse papillomavirus (MmuPV1) as a model to study cellular immune response to papillomavirus-induced neoplastic disease indicated that K17 overexpression contributed to persistent viral infection and papillomatosis by downregulating T cell infiltration (13). We also observed an inverse correlation between the level of K17 expression and the expression of CD8a and IFNγ-related genes at the RNA level when we interrogated head and neck squamous cell carcinoma (HNSCC) tumor RNA-Seq data from the Cancer Genome Atlas (TCGA) (13). Because K17 overexpression

has been reported in a wide range of cancer types, including ones that are not associated with any known viruses (9, 11), and because it was found to contribute to carcinogenesis in non-virally induced Gli2 transgenic mice (6), we hypothesize that K17 contributes to HNSCC growth by suppressing T cell infiltration, regardless of HPV status. Currently, two anti-PD1 immune checkpoint blocking antibodies, nivolumab and pembrolizumab, are FDA-approved to treat recurrent squamous cell carcinoma of the head and neck region, albeit with a response rate of less than 20% (14). High T cell infiltration in a patient's tumor is associated with better response to immune checkpoint therapy (15). In this study, we asked if K17 expression plays a role in resistance to immune checkpoint blockade therapies in HNSCC.

To test our hypotheses and validate the link between K17 expression and CD8+ T cells via RNA expression level, we analyzed a HNSCC tissue microarray (TMA) for K17 and CD8 protein levels, and correlated K17 expression level with patients' overall survival. To test how K17 mediates immune evasion of HNSCC *in vivo*, we utilized a syngeneic mouse HNSCC line, MOC2, derived from a chemical carcinogen-induced oral cavity tumor arising in C57BL/6 mice (16). MOC2 cells, when injected subcutaneously into syngeneic immunocompetent C57BL/6 mice, form fast growing tumors that are immunologically "cold", with limited T cell infiltration and low predicted neoantigen levels, and are resistant to combined immune checkpoint blockade treatment (anti-CTLA4+anti-PD1) (17, 18). We investigated whether knocking out K17 can turn an immunologically cold tumor into an immunologically hot tumor and whether MOC2 tumors would have increased responsiveness to immune checkpoint blockade treatment in the absence of K17. To confirm our hypothesis with human patient data, we also evaluated the K17 expression level in a cohort of HNSCC patients who received Pembrolizumab. These studies demonstrate that K17 contributes to immune evasion and to resistance to checkpoint blockade therapy in HNSCC and lead us to hypothesize that K17 is a strong predictive biomarker for HNSCC patients whose tumors are resistant to immune checkpoint blockade therapy.

Methods

Tissue microarray

Oropharynx squamous cell carcinoma tissue microarray (TMA) # 3 sections were provided by the Wisconsin Head and Neck Cancer SPORE. This TMA section contains 525 cores from 107 oropharynx squamous cell carcinoma, both HPV positive and HPV negative carcinoma; each sample is represented in triplicate 0.6 mm cores. The cancer cores include 171 primary, 207 lymph node metastatic, 6 distant metastatic, and 141 recurrent cancer cores. The tissue microarray (TMA) section was deparaffinized and blocked with 5% Goat serum. Antigens were retrieved in boiling 10 mM citrate buffer for 20 min. Tissues were then washed and stained overnight at 4 ˚C with anti-K17 (Abcam 109725), anti-CD8 (BioRad MCA351GT), anti-E-Cadherin (Abcam ab231303). Tissues were washed and stained with secondary antibodies conjugated with Alexa 488, Alexa 546 and Alexa 647. Tissues were washed and stained with Hoechst Dye before mounting in ProLong™ Diamond Antifade Mountant. The stained TMA was scanned by Vectra Automated Quantitative Pathology Imaging System at 20x objective. Scanned images were analyzed

using inForm software (PerkinElmer). The software was trained using nine scanned images to distinguish tumor compartment (marked by positive E-Cadherin staining) and stromal compartment (marked by negative E-Cadherin staining). Each fluorescence channel was then analyzed within each compartment.

HNSCC patient cohort evaluated for K17 expression level by IHC

Patients diagnosed with squamous cell carcinoma (SCC) of the head and neck region that were treated with immune checkpoint inhibitors (ICI) as part of routine clinical management at the University of Wisconsin-Madison were included in this study. Patient eligibility criteria included pathologic confirmation of SCC, treatment with at least one dose of anti PD-1 drug pembrolizumab, available baseline patient and disease information, and sufficient archival tissue available for analysis. Demographic, clinical, radiographical and treatment data for each patient were obtained from retrospective chart review. Initially, 37 patients were identified, however, only 26 patients had sufficient tissue and data available for analysis.

Human study endpoints

The primary end-point was disease control rate (DCR), i.e. the percentage of patients with radiographic response or stable disease as a result of their therapy. Radiological response assessments were not available for all enrolled patients and we did not wish to exclude patients without radiological reassessment. Therefore, the DCR was investigator-assessed (TL) for all patients with at least one post-treatment scan or evidence of clinical progression after treatment initiation. Progressive disease included radiographic and/or clinical progression. Clinical progression was defined by deterioration of performance status leading to best supportive care/hospice or death in patients without restaging scans available at the time of analysis. Secondary endpoints included progression-free survival (PFS) and overall survival (OS). PFS was defined as the time from initiation of treatment to the time of progression or death due to any cause, while OS was defined as the time from initiation of treatment until time of death or date of last follow up.

K17 immunohistochemistry and quantification

Formalin-fixed, paraffin-embedded tumor specimens from surgical resections were obtained from the archive of the Department of Pathology, sectioned into 4-μm-thick paraffin sections and deparaffinized according to standard procedures before being processed for IHC staining. Deparaffinization was carried out on the instrument, as was heat-induced epitope retrieval in the form of “cell conditioning” with CC1 buffer (Ventana, #950–224), an EDTA based buffer pH 8.4, for 32 minutes at 95○C. IHC for K17 (Anti-Cytokeratin 17, Rabbit Monoclonal, Clone EP1623, dilution 1:100, ab109725, Abcam, Cambridge, United Kingdom) was performed on an automated stainer (Ventana Discovery Ultra BioMarker Platform (Roche, USA)) following the manufacturer’s instructions. Semi-quantitative evaluation of K17 expression levels using brightfield microscopy was performed by two surgical pathologists (MBF, JX). Initially, an independent, blinded review was performed. The staining intensity (1+, 2+, 3+), percentage of tumor cells with K17 cytoplasmic staining, and distinct staining patterns were determined. Non-invasive precursor lesions, immune cells, nuclear staining, necrotic cells, and debris were excluded. Cases were categorized

into K17 high vs. low defined as >5% strong (3+) cytoplasmic staining intensity of tumor cells observed in the invasive carcinoma component. Cases with strong (3+) cytoplasmic staining intensity in >5% of tumor cells were grouped as high expressors. Cases with low or moderate staining intensity and low percentage of tumor cells with cytoplasmic staining were grouped as low expressors. Some staining patterns (mosaic/basal, perinuclear, golgi expression pattern) were interpreted based on combined IHC and clinicopathologic correlation, and were grouped as low expressors.

Animals

Wildtype C57BL/6 mice and Cas9 knock-in mice (constitutive Cas9-expressing mice; JAX stock #026179) on C57BL/6 background were obtained from Jackson and bred for this study. NOD-scid IL2Rgamma-null (NSG) mice were bred in University of Wisconsin-Madison animal breeding core. All mice were housed in the animal facility in aseptic conditions in micro-isolator cages and experiments carried out under an approved animal protocol. Six- to eight-week-old mice were used for experiments with the same ratio of males and females in each group. For T cell depletion experiment, 100 μg of anti-CD4 (BioXCell, clone GK1.5) and 100 μg of anti-CD8 antibody (BioXCell, clone 2.43) or 100 μg of isotype control (BioXCell, Rat IgG2b, κ) was delivered by intraperitoneal injection twice weekly, starting 1 day before tumor cell injection throughout the study. For detection of CD4 and CD8 depletion, CD8a FITC (Tonbo ebioscience, clone 53–6.7), CD4 PE (Tonbo ebioscience, clone RM4–5) were used for flow cytometry. For CXCR3 blocking experiment, 400μg of anti-CXCR3 (BioXCell, clone CXCR3–173) or isotype control antibody (BioXCell, Armenian Hamster IgG) was delivered i.p. three times a week, starting 1 day before tumor cell injection, throughout the study.

Cell line

MOC2 cell line was a gift from Dr. Ravindra Uppaluri from Dana-Farber Cancer Institute. MOC2 cells were maintained in F media: 1 part of DMEM+3 parts of F12 media supplemented with 5% FBS, EGF, pen/strep, cholera toxin, insulin, adenine and hydrocortisone. Passage number 15–60 were used for experiments for a maximum culture time of 6 months. Cell line authentication was not performed. Cells were tested mycoplasma negative. Guide sequences targeting Exon1, Exon4 and Exon5 of mouse KRT17 gene were designed using the Zhang lab's CRISPR guide website: zlab.bio. Annealed oligos containing the designed gRNAs were then ligated into the BsmBI site of LentiCRISPRv.2 and sequence was verified. Lentivirus was made by transfecting 293^{FT} cells with gRNA targeting plasmid, psPAX2 and VSV-g containing plasmids. Lentivirus was then collected 48 hours post transfection and used to infect MOC2 cells. Infected cells were then placed under puromycin selection (5μg/ml). Pooled cells were verified by immunofluorescence staining and qRT-PCR for K17 expression.

Flow cytometry

Subcutaneous tumors were trimmed of surrounding tissues and harvested on ice in PBS. Tumors were cut into 1 mm pieces and digested in 5 mL HBSS supplemented with 5% fetal bovine serum (FBS), 2 mM CaCl2, 2 mM MgCl2, 1 mg/ml collagenase D (Roche) and 200U/ml DNase I (Roche), at 37˚C for 30 min. Tissues were then homogenized with

the back of 1 ml syringe, passed through 0.7 μM filter and washed twice with cold PBS. Blood samples were collected from submandibular bleeding directly into red cell lysis buffer (Tonbo Biosciences) and incubated at room temperature for 10–15 min. Blood cells were then spun down and washed with PBS. Single cell suspensions were then stained with 1 μl Ghost Dye Violet 510 (Tonbo Biosciences) in 1 ml of PBS at 4˚C for 30 min. Samples were then washed with PBS supplemented with 2% FBS, blocked with anti-mouse Fc receptor antibody and stained with cell surface markers. Cells were then washed and fixed with fixation buffer (eBioscience) overnight at 4 ˚C. Cells were washed in PBS supplemented with 2% FBS and analyzed with ThermoFisher Attune. Flow cytometry beads (eBioscience) stained with each antibody were used as single-color controls. A combination of selected antibodies (anti-mouse) was used depending on the purpose of each study: CD45 APC-Cy7 (Biolegend, clone 30-F11), CD8a FITC (Tonbo ebioscience, clone 53–6.7), CD4 PE (Tonbo ebioscience, clone RM4–5), Gr1 PE-Cy5 (Biolegend, clone RB6–8C5), F4/80 BV421 (Biolegend clone BM8), CD11b BV605 (Biolegend, clone M1/70), CD11c PE-Cy7 (Biolegend, clone N418), NKp46 BV711 (Biolegend, clone 29A1.4).

Immunofluorescent staining

Tumors were cut in half and embedded in optimal cutting temperature compound (OCT) and frozen on dry ice before storing at −80 ˚C. Frozen tissues were the sectioned (5 microns thick) using a cryostat. Tissue slides were fixed in cold methanol in −20 ˚C for 10 min, washed with PBS +0.01% Triton X-100, then pure PBS, blocked with 5% goat serum at room temperature for 1 hour, and stained with purified primary antibody at 4˚C overnight. Tissues were then washed with PBS three times, stained with secondary antibodies at room temperature for one hour, counterstained with Hoechst Dye and mounted in Prolong mounting media (Thermo Fisher Scientific). The following antibodies were used for detecting mouse antigens by immunofluorescent staining: CD4 (eBioscience, clone RM4–5), CD8 (eBioscience, clone 53–6.7), K14 (eBioscience, polyclonal Cat#PA5–16722), K17 (provided by Pierre A Coulombe [57]), Goat anti-rabbit AlexaFluor647 (Molecular Probes), Goat anti-rat AlexaFluor 488 (Molecular Probes).

RNA sequencing

Fresh tumors were snap frozen in liquid nitrogen, placed into tissueTUBE (Covaris) and pulverized Cryoprep Pulverizer (Covaris). Total RNA was isolated by addition of 1ml or TRizol (Thermo Fisher Scientific) using RNA-binding columns (Qiagen RNA isolation kit). On column-bound RNA was treated with RQ1 RNase-free DNase (Promega) for 30 min at room temperature, washed with washing buffers, and eluted in RNase-free water. Pooled libraries were sequenced on Illumina NovaSeq 6000. RNA-Seq analysis was done using R and Bioconductor analysis framework. RNA short reads were preprocessed using FastQC (19) to screen for adapter sequence contamination and per-base and per-read quality assessment and then mapped to mouse genome mm10 using subread-align v1.5.3 (20). Short reads overlapping with gene annotation (NCBI RefSeq) were annotated using featureCount (21)for downstream analysis. Differential expressed genes were called with log2FC cutoff 2, and FDR-adjusted p-value <0.05 using linear model analysis (function voom from limma package) (22) with scaling normalization factors estimated using edgeR (23). Heatmap

of DE genes were generated using ComplexHeatmap package (24). Gene set enrichment analysis (GSEA 3.0) was done with genes that have a human homolog (ENSEMBL).

Single cell RNA sequencing

Tumors were collected and sorted for 150,000 live CD45+ cells per sample. Duplicate tumors were collected for each genotype. Around 6000 cells per sample were captured for library preparation, and sequenced on Illumina NovaSeq at the UW-Madison Biotechnology Center. Raw reads were aligned to the mm10 reference genome together with UMI (unique molecular identifier) counting using the Cell Ranger pipeline (v3) from 10X Genomics. Data was filtered using DoubletFinder (25) to remove potential doublets. Further filtering includes only the cells with low mitochondria contents (<=10%) and more than 200 genes covered by the mapping. To integrate the scRNA-Seq, we used a fuzzy clustering-based integration method (Harmony method) (26) to account for potential technical variance across samples. Downstream analysis for all CD45+ cells and for only myeloid cells were based on Seurat single-cell analysis package (27) including: principal component analysis with standard deviation saturation elbow plot to select the optimal number of principal components, graph-based clustering using *FindCluster* with different resolution from 0.1 to 2 to justify the number of clusters based on representative markers overlaid in the hierarchical tree across different resolution (*clustree* R package), differentially expression analysis using MAST (28) implemented in Seurat with the cutoff average log2FC 0.25, and at least 25% of cell expressed the markers. Visualization with heatmap, DotPlot, and violin plot was done using Seurat in R and Bioconductor platform.

To infer ligand/receptor interactions between different immune cells in MOC2 vs. MOC2K17KO tumors, we used CellphoneDB version 2.1.7 (29) with the default parameters. Only interactions with p value < 0.05 from the permutation test were considered further for analysis. We used Single-Cell Regulatory Network Inference and Clustering method, pySCENIC to infer transcription factor gene regulatory networks (30). The regulons were identified from co-expression of transcription factors and their target genes from the RCisTarget database (https://github.com/aertslab/RcisTarget). We ran pySCENIC version 0.11.2 using default parameters. We then used a generalized linear model to identify top regulons that are differentially expressed in MOC2 and MOCK17KO (FDR-corrected p values < 0.05) tumors in different immune cell-types based on the AUC scores estimated from pySCENIC .

qRT-PCR

500 ng of RNA from each sample were used for cDNA synthesis using Quantitect reverse transcription kit (Qiagen). SYBR Green or TaqMan probe were then used for quantitative PCR performed on ABI 7900HT, all gene expression levels were normalized to GAPDH. The following primers were used for SYBR Green detection of mouse gene expressions: GAPDH forward 5’- CATGGCCTTCCGTGTTCCTA-3’; GAPDH reverse 5’- GCGGCACGTCAGATCCA-3’; CXCL9 forward 5’- TCCTCTTGGGCATCATCTTCC-3’; CXCL9 reverse 5’- TTTGTAGTGGATCGTGCCTCG-3’; CXCL10 forward 5’- CCAAGTGCTGCCGTCATTTTC-3’; CXCL10 reverse 5’- GGCTCGCAGGGATGATTTCAA-3’; CXCL11 forward

5’- GGCTTCCTTATGTTCAAACAGGG-3’; CXCL11 reverse 5’- GCCGTTACTCGGGTAAATTACA-3’; PD-L1 forward 5’- CCAGCCACTTCTGAGCATGA-3’; PD-L1 reverse 5’- CTTCTCTTCCCACTCACGGG-3’; IFNγ forward 5’- ACAATGAACGCTACACACTGCAT-3’; IFNγ reverse 5’- TGGCAGTAACAGCCAGAAACA-3’. The following TaqMan probes (Thermo Fisher Scientific) were used for K17 expression measurement: GAPDH (Mm99999915_g1); K17 (Mm00495207_m1).

Statistics

All statistical analyses for animal studies were done with Graphpad Prism. Two-way ANOVA was used for statistical comparison when two variables (tumor growth time and genotype) were involved. When some mice were found dead before the endpoint of study, a mixed-effects model (REML) was used to handle missing values. For single variable experiments, t test or one-way ANOVA was used for statistical comparison as indicated. For survival analyses, log-rank test was used for statistical comparison.

For survival analysis for human TMA and TCGA data, we used the Kaplan–Meier method with right censoring for testing tumor K17 expression and overall survival. We used the Survival package (version 3.2–13) for this analysis. A log-rank test was used to evaluate survival differences between low- and high- groups based on 25^{th} percentile top and bottom of expression values. Two-sided p values < 0.05 were considered significant.

The association between clinical response to Pembrolizumab and K17 expression was tested using the Fisher exact test. The PFS and OS outcomes were estimated using the Kaplan–Meier method with appropriate censoring, and the log-rank test was used to investigate differences between groups. Two-sided $p < 0.05$ was considered significant. There were some variations in the timing and interval of radiological assessment given the retrospective nature of this analysis. Therefore, DCR was investigator-assessed based on available imaging and clinical data. Results from this retrospective study should mainly be considered exploratory, so no correction for multiple testing was applied. Statistical analysis was performed using SPSS Statistics version 24 (IBM Corp).

Ethical Statement

The clinical data analysis was conducted in accordance with the Declaration of Helsinki and received institutional ethics approval from the University of Wisconsin-Madison (UW18144 with IRB#2018–1510), under a waiver of informed consent. Animal studies (Protocol M005871) were approved by the School of Medicine and Public Health Animal Care and Use Committee (IACUC) of the University of Wisconsin-Madison and conducted in accordance with the National Institutes of Health Guide for the Care and Use of Laboratory Animals.

Data Availability Statement: The data generated in this study are available within the article and its supplementary data files. The sequencing data generated in this study have been deposited to GEO (GSE182026 and GSE182002: unified under SuperSeries GSE182027), and have been made available to the public.

Results

Human head and neck cancers with high levels of K17 expression have shorter survival regardless of CD8+ cell level

To test whether K17 is overexpressed in human head and neck cancers at the protein level, and whether high K17-expressing cancers have low abundance of infiltrating CD8+ T cells, we performed immunofluorescence staining on a tissue microarray (TMA, Supplemental Table 1) containing both HPV+ and HPV- head and neck cancer patient specimens with K17, CD8 and E-cadherin specific antibodies. K17 mean fluorescence intensity (MFI) and CD8+ percent positivity were automatically calculated within or in close proximity to the E-cadherin+ regions (Figure 1A). TMA cores lost or damaged (e.g. folded) during processing, or cores with high autofluorescence (Supplemental Figure 1A) were excluded from analyses. We found that, samples that were high in K17 expression (z score > 1.64) all had less than 20% of intratumoral and peritumoral CD8+ T cell (blue box in Figure 1B), and, conversely, samples that had high level of CD8+ T cell infiltration (z score > 1.64) all had K17 MFI lower than 1.3 (red box in Figure 1B), demonstrating that K17 high expressing tissues and CD8+ high infiltrating tissues are mutually exclusive (Figure 1B, left). Interestingly, when we subclassified the tissue cores by their p16 status to distinguish HPV+ (p16+) from HPV- (p16-) cancers, we found HPV- samples had higher K17 expression and lower CD8 level compared to HPV+ samples (Figure 1B middle and right). When we correlated survival time with K17 expression (average K17 expression from multiple primary cancers from the same patient), the highest 25% K17-expressing patients had significantly shorter survival than the lowest 25% K17-expressing patients (Figure 1C). Among the high K17-expressing patients, their survival were further stratified by their CD8+ level (Figure 1D left). The low K17-expressing patients had the best overall survival among all subgroups, regardless of intratumoral and peritumoral CD8+ level (Figure 1D). Our analysis of K17 and CD8a RNA expression in the TCGA head and neck cancer patient RNA-seq data showed that, as seen with the TMA, tumors expressing high levels of K17 are mutually exclusive from tumors expressing high levels of CD8 (Supplemental Figure 1B). Also, as observed with the TMA data, the HPV- cancers had higher levels of expression for K17 than HPV+ cancers (Supplemental Figure 1B). However, K17 RNA level did not correlate with survival (Supplemental Figure 1C). This suggests to us that measurement of K17 at the protein level and within the tumor-specific region may be necessary for it to be used as a prognostic marker. These human patient data reveal that K17 is highly expressed in a subset of both HPV+ and HPV- human head and neck cancers, and, when scored at the protein level, is associated with poor survival in these patients. Because patients with HPV- HNSCC have higher K17 expression and lower CD8 level, we focused our studies on this cancer type.

K17 supports MOC2 *in vivo* growth in immunocompetent mice but is not required for growth in immunodeficient mice

MOC2 represents a valuable syngeneic (C57BL/6) mouse head and neck cancer model for our studies because it represents an immunologically cold tumor phenotype and it expresses K17 (Figure 2A and 2B). We designed CRISPR/Cas9 guide sequences targeting Exon 1, Exon 4 and Exon 5 of the mouse K17 gene to generate three independent K17 knockout (K17KO) MOC2 cell bulk populations that were expanded from the parental cells that had

been transduced with a retroviral vector that expressed Cas9 together with the appropriate guide RNA. These bulk populations were maintained under drug selection during their culture *in vitro* and were found to have undetectable K17 protein expression (Figure 2A and 2B) and very low levels of K17 mRNA (Figure 2C). When subcutaneously injected into immune-deficient NOD scid gamma (NSG) mice, one of the three K17KO MOC2 cell lines grew slightly faster than the parental wildtype MOC2 cells, with a 100% growth incidence, while the other two K17KO MOC2 cell lines formed tumors that grew nearly identically to tumors arising in mice injected with parental MOC2 cells (Figure 2D). Mice bearing K17KO MOC2 lines had similar survival compared to those bearing MOC2 tumors (Figure 2D), suggesting that knocking out K17 did not reduce the tumorigenicity of MOC2 cells. However, when injected into syngeneic, immunocompetent, C57BL/6 mice, all three K17KO MOC2 cell lines had significantly delayed growth (Figure 2E), with a 50% complete rejection rate on average (Figure 2F). The K17KO-3 cells had the lowest rejection rate among the three K17KO lines generated. We believe this might be because bulk populations retained cells in which K17 was not successfully knocked out and these K17+ cells then expanded *in vivo*, during which time the cells could not be maintained under drug selection, as evidenced by the presence of K17+ tumor cells in the resulting tumors from bulk populations (green cells in Supplemental Figure 2A). For this reason, we went back and generated single cell clones of K17KO-3 that were confirmed to be K17-negative by western blot analysis (Supplemental Figure 2B). When these cells were injected into syngeneic mice, 100% of the tumors were rejected (Supplemental Figure 2C), consistent with our hypothesis that leaky expression of K17 in the bulk populations likely contributed to variable levels of rejection. The observed, delayed growth of K17KO MOC2 tumors was unlikely due to Cas9 expression in K17KO MOC2 cells, because K17KO MOC2 tumors had comparable delayed growth and rejection rates in Cas9 Knock-in (Cas9KI) mice that do not recognize Cas9 as a foreign antigen (Supplemental Figure 2D and 2E), and because K17KO MOC2 tumors grew significantly slower than MOC2 cells expressing Cas9 only (Supplemental Figure 2F). Flow cytometry of remaining K17KO MOC2 tumors and parental MOC2 tumors revealed significantly higher numbers of CD45+, CD4+ and CD8+ immune cell infiltrates in K17KO MOC2 tumors (Figure 2G, Supplemental Figure 2G). Infiltration of CD8+ T cells was confirmed by immunofluorescence staining (Figure 2H). These data are consistent with the hypothesis that K17 inhibits immune-mediated spontaneous rejection of head and neck cancer cells in immunocompetent mice and that ablation of K17 expression creates an immunologically hot tumor microenvironment.

Next, we performed RNA sequencing (RNA-Seq) of bulk RNA extracted from the persisting, slow growing K17KO MOC2 tumors as well as parental MOC2 tumors from C57BL/6 mice. We identified 115 downregulated genes and 388 upregulated genes (adjusted $p<0.05$, $\log2FC < -2$ or > 2) in K17KO MOC2 tumors compared to MOC2 tumors. Among the upregulated genes, we observed active cellular immune response genes, including CD8a, CD28, Grzmb, Batf3, and CXCL9 (Figure 2I). Gene Set Enrichment Analysis (GSEA) (31) defined seven upregulated pathways in K17KO MOC2 tumors that were all related to immune response, including IFN alpha and IFN gamma responses (Figure 2J). We confirmed upregulation of IFNγ-related gene expression by qRT-PCR analyses of the bulk tumor RNA, including IFNγ, CXCL9 and PD-L1 (Figure 2K). On the other hand, the top

enriched pathways in downregulated genes were cell cycle and cell proliferation-related, including E2F targets, MYC targets and mitotic spindle-associated genes (Figure 2J). These findings were consistent with the delayed growth kinetics of K17KO MOC2 tumors in the C57BL/6 mice (Figure 2E). Overall, the RNA-Seq data provide strong evidence for a major switch in the immune signature of MOC2 vs K17KO MOC2 tumors, with K17KO tumors possessing a more activated T cell and immunogenic tumor microenvironment that correlates with a strong reduction in cell growth parameters.

T cells are responsible for rejection of K17KO MOC2 cells in C57BL/6 mice

Based on our data described above, we hypothesized that infiltrating T cells were responsible for the rejection and slow growth of K17KO MOC2 tumors in syngeneic, immunocompetent mice. We therefore depleted CD4+ and CD8+ T cells from C57BL/6 mice beginning at three days post injection of K17KO MOC2 cells and continued depleting these cells through the time course of the study. We found that none of the K17KO MOC2 tumors were rejected in mice depleted for T cells, and that these tumors grew significantly larger than the K17KO MOC2 tumors growing in mice treated with isotype control antibodies (Figure 3A). The absence of T cells in the K17KO MOC2 tumors growing in T cell-depleted mice was confirmed by flow cytometry (Figure 3B, Supplemental Figure 3). These data confirm the hypothesis that the spontaneous rejection of K17KO MOC2 tumors in immunocompetent C57BL/6 mice is T-cell dependent.

Because we observed increased levels of CXCL9 and CXCL11 RNA expression, chemokines that attract activated CXCR3-expressing T and NK cells, in K17KO MOC2 tumors (Figure 2K), we tested whether CXCR3 was important in the rejection of K17KO MOC2 tumors *in vivo*. Anti-CXCR3 antibody was delivered to mice by i.p. to block CXCR3's interactions with its ligands one day before injection of K17KO MOC2 cells. In isotype control treated mice bearing K17KO MOC2 tumors, the tumors grew significantly slower than K17KO MOC2 tumors in CXCR3-blocked mice (Figure 3C). Blocking CXCR3 also significantly delayed the rejection of K17KO MOC2 tumors (Figure 3D). However, blocking CXCR3 did not completely abrogate the anti-tumor immune effect against K17KO MOC2 tumors, as they still grew more slowly than the parental MOC2 tumors (Figure 3C); even with CXCR3 blockade two K17KO MOC2 tumors were completed rejected (Figure 3D), suggesting there are other factors that contribute to rejection of K17KO MOC2 besides CXCL9/CXCL11 and CXCR3 interactions.

K17KO MOC2 cell-immunized mice generate partially protective memory responses against parental MOC2 cells

To test if the immune response elicited by K17KO MOC2 cells are not solely caused by potential neoantigens resulting from CRISPER/Cas9 editing, we re-challenged those C57BL/6 mice that were able to completely clear K17KO MOC2 cells ('K17KOMOC2-immuned mice') with parental MOC2 cells. We found that half of the immunized mice were able to completely reject parental MOC2 tumor growth, while none of naïve mice rejected parental MOC2 tumors (Supplemental Figure 4A, left). We also observed a slightly but not significantly delayed growth of MOC2 tumors in the K17KOMOC2-immunized mice (Supplemental Figure 4A, right). When we analyzed splenocytes from K17KOMOC2-

immunized mice and naïve mice upon MOC2 tumor challenge, we found an increased number of CD4+ and CD8+ T cells that had memory markers (CD62L- CD44 high and CD62L+ CD44 high) (Supplemental Figure 4B and 4C). These data indicate that the immune response elicited by K17KO MOC2 cells are able to exert partial protection against parental MOC2 tumor challenge, suggesting that K17KO MOC2-induced immune responses are able to recognize antigens present in parental MOC2 cells.

K17KO MOC2 tumors have enhanced response to immune checkpoint blockade treatment

Next, we tested whether the immunologically hot K17KO tumors had increased response to immune checkpoint blockade treatment. At day 14 post injection, about half of K17KO MOC2 tumors were completely rejected. K17KO MOC2 tumors that were larger than 2mmx2mm on day 14 were defined as tumors that survived natural immune surveillance because they continued to grow over time. C57BL/6 mice carrying these > 2mmx2mm, persisting K17KO MOC2 tumors were treated with anti-PD1+anti-CTLA4 antibodies or isotype controls starting at 14 days post-injection of the tumor cells. Isotype control treated K17KO MOC2 tumors either continued to grow or maintained the same size for three weeks and started to grow in size after day 35 post-injection (Figure 4A). In contrast, all five anti-PD1+anti-CTLA4-treated K17KO MOC2 tumors completely regressed by day 45 post-injection (Figure 4A). On the other hand, the parental MOC2 tumors that were treated at the same time (day 14 post injection) did not respond to anti-PD1+anti-CTLA4 treatment (Figure 4B). Due to the significant difference in size of K17KO MOC2 tumors versus MOC2 tumors at the time we initiated immune checkpoint blockade treatment, we also treated a cohort of mice bearing parental MOC2 tumors that had a size similar to that of the K17KO MOC2 tumors, starting at day 6 post injection. One out of five MOC2 tumors treated from day 6 post injection had a complete response, one MOC2 tumor had a delayed growth, the other three MOC2 tumors continued to grow despite ICB treatment (Figure 4C). Therefore, we conclude that, even when accounting for initial tumor size, the rejection of tumors in response to immune checkpoint blockade treatment is significantly higher for K17KO MOC2 tumors (CR: 5/5, Figure 4A) compared to parental MOC2 tumors (CR: 1/5, Figure 4C) ($p<0.05$, Fisher's exact test).

To test whether anti-PD1+anti-CTLA4-treated mice bearing K17KO MOC2 tumors that then regressed generated protective memory response to parental MOC2 cells, we rechallenged the five mice that completely cleared K17KO MOC2 upon immune checkpoint blockade treatment ('K17KO-cured mice'), as well as twenty-four mice that spontaneously cleared K17KO MOC2 tumors ('K17KO-immunized'), with parental MOC2 cells. MOC2 tumor growth was significantly delayed in both K17KO-immunized mice and K17KO-cured mice compared to naïve mice (Figure 4D). Among these mice, 65% of the K17KO-immunized mice were able to completely reject MOC2 tumor growth, versus 80% of ICB-treated, K17KO-cured mice (Figure 4E). CD62L and CD44 analyses of splenocytes from these mice indicated that higher numbers of CD4+ and CD8+ T cells with memory phenotypes were present in the immunized mice compared to naïve mice (Figure 4F). Altogether, these data demonstrate that the formation of memory response against MOC2 tumors occurred in both K17KO-immunized mice and K17KO-cured mice, with no significant difference in protection against MOC2 challenge. Interestingly, the frequencies of CD11b+Gr1 high and

CD11b+Gr1 low cells were higher in the spleens of mice that were unable to reject MOC2 tumors (tumor-bearing), compared to the spleen of mice that rejected MOC2 tumors (tumor free) (Figure 4G, Supplemental Figure 5), indicating that myeloid-derived suppressor cells might play a role in supporting MOC2 tumor outgrowth in K17KO-immunized mice.

High level of K17 expression in HNSCC patients is associated with poor response to Pembrolizumab

To investigate the human relevance of our findings that K17 status influences response to ICB in mice, we evaluated K17 expression by immunohistochemistry in a cohort of 26 HNSCC patients receiving Pembrolizumab (Supplemental Table 2) and looked for whether there was a correlation between their level of K17 expression and their clinical response. Based on high expression cut-off of >5% strong cytoplasmic staining of tumor cells, 18 (69.2%) patients had K17 high expressing tumors and 8 (30.8%) had K17 low expressing tumors (Figure 5A and Supplemental Figure 6). Disease control rate was significantly associated with K17 expression status ($p<0.001$, Figure 5B). In the K17 high group, all patients had progressive disease. In the K17 low group, 6 patients (75%) had disease controlled, while 2 (25%) patients had progressive disease. In addition, K17 low patients had significantly longer overall survival ($p=0.02$, Figure 5C) and progression-free survival ($p=0.004$, Figure 5D). These clinical data support our hypothesis that high K17 expression in head and neck cancers confers resistance to ICB therapy.

K17KO MOC2 tumors have switched tumor immune microenvironment phenotypes

Although we observed partial abrogation of the immune-mediated anti-tumor effect against K17KO MOC2 tumor growth with anti-CXCR3 blocking antibody, there was still a significant growth delay of K17KO MOC2 tumors in CXCR3-blocked mice compared to parental MOC2 tumors (Figure 3C). These results prompted us to use scRNA-Seq to compare in-depth the immune landscapes of K17KO MOC2 tumors prior to complete regression to that of parental MOC2 tumors . ScRNA-Seq analysis of CD45+ cells between K17KO MOC2 and MOC2 tumors revealed a higher abundance of myeloid cells in MOC2 tumors (compared to K17KO tumors), with neutrophils as the most abundant immune cell-types compared to lymphoid cells (T and B cells) and NK cells (Figure 6A-C). We observed increases in all 3 major T cell subsets (CD4+, CD8+ T cells and regulatory T cells Treg) with a much higher CD4/Treg and CD8/Treg ratios in the K17KO MOC2 tumors. Subset analysis of NK cells led to identification of two NK cell subsets (Supplemental Figure 7A). NK cell subset 1 expresses Eomesodermin (Eomes), a crucial transcription factor required for NK cell maturation (32), as well as Ly49 receptors (Klra4, Klra8, Klra9) and integrin CD49b (Itga2), which are markers for mature NK cells (Supplemental Figure 7B-C). The NK cells from K17KO MOC2 tumors are skewed towards a more mature phenotype (Supplemental Figure 7B-C), suggesting a tumor microenvironment that supports NK cell maturation. Analysis of CXCR3 expression on immune cell subsets (Supplemental Figure 8) showed that CXCR3 is more abundantly expressed in CD8+ T cells from K17KO MOC2 tumor, but no difference was observed for other T cell and NK subsets. These data indicate that the increased CD8+ T cell infiltration in K17KO MOC2 cells could be due to increased CXCR3 expression on CD8+ T cells. Given reported heterogeneity of myeloid cells in the tumor microenvironment, we further clustered and identified 4 DC

subsets (including pDCs) and 5 macrophage subsets including 1 subset expressing CXCL9 (Figure 6D, Supplemental Figure 9). Interestingly, we saw an opposite trend of enrichment of cDC1 and cDC2 subsets in MOC2 vs. K17KO MOC2 tumors. While cDC1 was slightly decreased in frequencies in K17KO MOC2 tumors, cDC2 that expressed monocyte gene signatures were more abundant in K17KO MOC2 samples. Moreover, we observed diversity in macrophage subsets, with M1-like subsets (Mac_CXCL9, Mac_CX3CR1), frequencies of which were increased, and M2-like subset (Mac_Trem2, Mac_Fn1) frequencies of which were decreased in K17KO MOC2 tumors (Figure 6E). Together, the data show a potentially multifaceted mechanism by which K17 mediates immune evasion in MOC2 tumors.

Discussion

K17 has been reported as a negative prognostic marker in breast cancer, oral cancer, cervical cancer and ovarian cancer (7, 9–11, 33). In addition, K17 identifies with the most lethal molecular subtype of pancreatic cancer (34). However, how K17 contributes to cancer pathogenesis and worse prognosis is not fully understood. Our analysis of HNSCC tissue microarray, together with our mouse data in this report, provide new insight in the role of K17 in immune evasion and its contribution to cancer pathogenesis. In our TMA data as well as TCGA data analyses, there are still a large number of patients who had low K17 expression that also had low level of CD8 infiltrating T cells, suggesting the overexpression of K17 is just one of many mechanisms that mediates immune evasion by cancers.

Despite being a negative prognostic marker in cancer, the role of K17 in metastasis is more controversial. In a pancreatic cancer model, Zeng et al. have shown that K17 acts as a tumor suppressor and inhibited cancer cell migration and invasion *in vitro* (35). By inhibiting K17 in pancreatic cancer cells, they observed increased tumor growth in immunodeficient mice (35). A more recent study by Escobar-Hoyos's group, on the other hand, showed K17 solubilization and nuclear localization enhances tumor growth and metastatic potential using an isogenic murine PDAC model (36). Both of these studies were performed in immunodeficient mice, where the effect of immune response had been excluded. To further investigate the role of K17 in cancer metastasis, an immunocompetent model should be considered.

When we knocked out K17 from MOC2 tumors, we found they could still grow aggressively in immunodeficient mice, indicating K17 was not necessary for their tumorigenicity, but it was important for establishing their growth in immunocompetent mice. Despite upregulated IFNγ response in K17KO MOC2 tumors growing in C57BL/6 mice, we also found upregulated PD-L1 and CTLA4 in these tumors, suggesting higher CTLA4 and PD-L1 expression may be a result from K17KO MOC2 tumors evading immune response and supporting their persistent growth *in vivo*. The most clinically significant observation with this mouse model was that K17 confers resistance to immunotherapy (Figure 4). Importantly, we found the same to be true in human head and neck cancer patients (Figure 5).

In cancer patients receiving anti-PD1 therapies, PD-L1 has been identified as a biomarker predictive of response. However, controversies have arisen using PD-L1 as a reliable marker

for ICB response (37–39) with some anti-PD1 drugs having been approved for treatment of PD-L1 negative cancers too. The results of our exploratory retrospective analysis of 26 HNSCC patients treated with ICB suggest a strong association between K17 status as determined by immunohistochemistry and clinical benefit from ICB therapy, as well as all investigated time-to-event endpoints. Associated challenges were the heterogenous staining in several cases (Supplemental Figure 6). Limitations of this analysis are the small sample size and the retrospective nature of the study with associated lack of comprehensive radiologic assessment. Considering the unmet need for predictive biomarkers of response to ICI in HNSCC and the shortcomings of PD-L1 status in this patient population (40), our work supports further validation studies in larger cohorts and in a prospective setting.

Among the 26 HNSCC patients analyzed, 14 of them had available data for PD-L1 expression level. Eleven of them had high PD-L1 expression, and 3 of them had low PD-L1 expression (Supplemental Table 2). We did not find a correlation between PD-L1 status and K17 expression level, or a correlation between PD-L1 status and their response to Pembrolizumab (Supplemental Table 3). More patients should be analyzed for their PD-L1 status in this cohort or in separate cohorts of patients to make a meaningful conclusion. Other recent work (41) showed that PD-L1 expression in macrophages and DCs are higher in the patients who responded to anti-PD1 therapy in breast cancer. Our bulk RNA-Seq data from mouse model showed upregulated PD-L1 RNA expression in K17KO MOC2 tumors (Figure 2I and 2K), and our scRNA seq data also showed upregulated PD-L1 expression in myeloid cells (Supplemental Figure 8), suggesting the upregulation of PD-L1 could be a result from the elevated level of IFNγ in the tumor environment because PD-L1 is an IFNγ-responsive gene. Whether K17 plays a direct role in regulating PD-L1 expression on tumors cells requires further investigation.

A potential limitation of this study is that we only used one mouse HNC model (MOC2) for our preclinical studies. MOC2 was chosen because it gives rise to immunologically cold, ICB-unresponsive tumors and, as we predicted based upon our prior studies in the context of papillomaviruses that cause cancer (13), was converted to immunologically hot, ICB-responsive tumors once we knocked out K17 (Figures 2E-K, Figure 4A). Importantly, our clinical studies in human HNC patients (Figures 1 and 5), confirmed the relevance of our findings with the MOC2 preclinical model. Nevertheless, other mouse HNC models do exist and may be informative. One other, commonly used mouse HNC model is MOC1. It gives rise to immunologically hot, ICB-responsive tumors and is characterized as having a high mutational burden, high MHC class I expression, and is sensitive to innate immune activation, which may drive its phenotype (17, 42, 43). Our own studies on MOC1 indicate that it does express K17, which was counter-intuitive given the preclinical and clinical data presented in this study. We are now engaged in learning if the immune-suppressive effects of K17 are compromised in MOC1 cells, as this may contribute insights into the mechanism of action of K17. One explanation is that the high mutational burden of MOC1 cells, which is predicted lead to higher numbers of neoantigens, overrides K17’s effects.

We have previously shown in the mouse papillomavirus (MmuPV1)-induced disease model, that CXCL9/CXCR3 axis was required for successful papilloma regression in K17KO mice (13). In this report, we observed a similar level of CXCL9 upregulation in the K17KO

MOC2 tumors. However, when we blocked CXCR3, we only partially rescued the growth of K17KO MOC2 tumors (Figure 3C and 3D). These results indicate that, in K17KO MOC2 tumors, CXCL9/CXCR3 is just one of multiple likely chemotaxis signals that contribute to T cell recruitment in K17KO MOC2 tumors. We have previously identified K14+ papilloma cells and macrophages as the major source of CXCL9 in MmuPV1-induced papillomas. Our preliminary *in vitro* results indicate that K17KO MOC2 cells, upon IFNγ stimulation, produce less CXCL9 than WT MOC2 cells (Supplemental Figure 10), which is consistent with what was published by Chung et al (44). These results suggest that K17KO MOC2 tumor cells do not directly contribute to the upregulation of CXCL9 in the tumor microenvironment, rather, other cellular sources of CXCL9, such as macrophages (Supplemental Figure 8), may contribute to the CXCL9-enriched environment. Increasing evidence points to a positive role of CXCL9-producing macrophages in fighting cancer and mediating response to ICB therapy. House et al. reported that CXCL9-producing macrophages were associated with more prolonged survival of melanoma patients who received ICB therapy and were essential for ICB efficacy in pre-clinical mouse models (45). Dangaji et al. (46) showed that in variety of human cancers, tumor-derived CCL5 expression and myeloid-derived CXCL9 expression correlated with higher CD8+ T cell infiltration in cancer patients and response to PD-1 blockade therapy. Recent work (47) shows that CXCL9 is the top predictive biomarker for ICB response in HNSCC patients based on gene-panel profiling from the whole tumors from clinical trial data performed by MERCK (48). Therefore, one of the possible mechanism by which K17 downregulates T cell infiltration is by suppressing CXCL9 production in macrophages through tumor cell-macrophage interactions.

In order to explore other potential mechanisms by which K17KO tumors pose anti-tumoral immune phenotypes, we performed the following two analyses of our scRNA-Seq datasets. First, we inferred ligand-receptor (LR) interactions between different immune cell-types in MOC2 versus K17KO MOC2 tumors by analyzing the scRNA-Seq using CellPhoneDB (29). We identified 15 LR interactions that are shared as well as 19 and 9 unique interactions in MOC2 and K17KO MOC2 tumors, respectively (Supplemental Figure 11A). Consistent with our other data (Figure 2 and Supplemental Figure 8), CellPhoneDB identified the CXCL9:CXCR3 interaction between macrophage and T cells was preferentially found in the immune cells infiltrating K17KO MOC2 tumors (Supplemental Figure 11B). We also identified the CCL7:CCR1 LR interaction to be uniquely present in K17KO MOC2 tumors. This ligand-receptor interaction is believed to recruit cDC1 dendritic cells to tumors to facilitate ICB response in non-small cell lung cancer (49). The most dominant LR interaction amongst immune cells in MOC2 tumors was CCL2:CCR2, which is known to be pro-tumoral in other tumor types such as breast cancer, hepatocarcinoma and melanoma (50, 51). The full list of interactions is shown in Supplemental Tables 4 and 5. Second, we sought to identify transcription factor networks differentially expressed in immune cells from MOC2 vs K17KO MOC2 tumors using SCENIC analysis (30) of our scRNA-Seq data sets. We generated a list of TFs that were overexpressed in immune cells from the K17KO MOC2 tumors (Supplemental Figure 11C). Interestingly, we found co-expression of leucine zipper ATF-like transcription factor (*Batf*) and interferon regulatory factor 4 (*Irf4*) in CD8 T cells. These factors were recently identified to counter T cell exhaustion in the

tumor microenvironment (52). Ongoing studies are underway to uncover which of these cell-cell signaling interactions and their downstream target gene expression networks are important in improving the ICB efficacy for K17KO MOC2 tumors, and how the expression of K17 in tumor cells lead to decreased immune response. These studies should provide new insights into how K17 expression facilitates evasion of tumors from immune surveillance and potentially identify new druggable targets that can enhance the efficacy of ICB therapy in patients with non-responsive tumors.

Supplementary Material

Refer to Web version on PubMed Central for supplementary material.

Acknowledgments

We thank Heather Geye and Shari Piaskowski for collecting clinical data for the TMA specimens. We thank Dr. Ravindra Uppaluri from Dana–Farber/Harvard Cancer Center for providing the MOC2 cells. We thank Dr. Pierre Coulombe (University of Michigan) for providing the K17 knockout mice and anti-mouse K17 antibodies. We thank Dr. Gopal Iyer (University of Wisconsin-Madison) for assistance with tissue pulverization. We would like to thank Dr. Howard H. Bailey and Dr. Hamid Emamekhoo for their assistance with clinical data interpretation. The author(s) utilized the University of Wisconsin – Madison Biotechnology Center's Gene Expression Center Core Facility (Research Resource Identifier - RRID:SCR_017757) for scRNA library preparation and the DNA Sequencing Facility (RRID:SCR_017759) for sequencing. The authors thank the University of Wisconsin Translational Research Initiatives in Pathology (TRIP) laboratory, supported by the UW Department of Pathology and Laboratory Medicine, UWCCC (P30 CA014520) and the Office of The Director- NIH (S10OD023526) for use of its facilities and services.

This research was supported by the 2020 AACR-Genentech Immuno-oncology Research Fellowship, Grant Number 20–40-18-WANG, the University of Wisconsin-Madison Carbone Cancer Center Transdisciplinary Cancer Immunology-Immunotherapy Pilot Grant, University of Wisconsin Head and Neck SPORE grant CEP award (P50DE026787 to H.Q.D), University of Wisconsin Head and Neck SPORE grant CEP award (P50DE026787 to M.B.F.) and grants from the National Institutes of Health (P01CA022443, R35 CA210807, P50 DE026787, R01 CA228543 to P.F.L.).

References

1. Paladini RD, Takahashi K, Bravo NS, Coulombe PA, Onset of re-epithelialization after skin injury correlates with a reorganization of keratin filaments in wound edge keratinocytes: defining a potential role for keratin 16. Journal of Cell Biology 132, 381 (1996). [PubMed: 8636216]
2. Hobbs R.P. DDJ, Jacob JT, Han MC, Chung BM, Batazzi AS, Poll BJ, Guo Y, Han J, Ong S, Zheng W, Taube JM, Čiháková D, Wan F, Coulombe PA, Keratin-dependent regulation of Aire and gene expression in skin tumor keratinocytes. Nature Genetics 47, 933–938 (2015). [PubMed: 26168014]
3. Komine M, Freedberg IM, Blumenberg M, Regulation of epidermal expression of keratin K17 in inflammatory skin diseases. J Invest Dermatol 107, 569–575 (1996). [PubMed: 8823363]
4. McGowan KM, Coulombe PA, Keratin 17 expression in the hard epithelial context of the hair and nail, and its relevance for the pachyonychia congenita phenotype. J Invest Dermatol 114, 1101–1107 (2000). [PubMed: 10844551]
5. McGowan K.M. CPA, Onset of keratin 17 expression coincides with the definition of major epithelial lineages during skin development. J Cell Biol 143, 469–486 (1998). [PubMed: 9786956]
6. DePianto D, Kerns M, Dlugosz AA, Coulombe PA, Keratin 17 promotes epithelial proliferation and tumor growth by polarizing the immune response in skin. Nature Genetics 42, 910–914 (2010). [PubMed: 20871598]
7. Escobar-Hoyos LF, Yang J, Zhu J, Cavallo JA, Zhai H, Burke S, Koller A, Chen EI, Shroyer KR, Keratin 17 in premalignant and malignant squamous lesions of the cervix: proteomic discovery and immunohistochemical validation as a diagnostic and prognostic biomarker. Mod Pathol 27, 621–630 (2014). [PubMed: 24051697]

8. Khanom R, Nguyen CTK, Kayamori K, Zhao X, Morita K, Miki Y, Katsube K, Yamaguchi A, Sakamoto K, Keratin 17 Is Induced in Oral Cancer and Facilitates Tumor Growth. PLOS One 11, (2016).
9. Merkin RD, Vanner EA, Romeiser JL, Shroyer ALW, Escobar-Hoyos LF, Li J, Powers RS, Burke S, Shroyer KR, Keratin 17 is overexpressed and predicts poor survival in estrogen receptor–negative/human epidermal growth factor receptor-2–negative breast cancer. Human Pathology 62, 23–32 (2016). [PubMed: 27816721]
10. Regenbogen E, Mo M, Romeiser J, Shroyer ALW, Escobar-Hoyos LF, Burke S, Shroyer KR, Elevated expression of keratin 17 in oropharyngeal squamous cell carcinoma is associated with decreased survival. Head and Neck 40, 1788–1798 (2018). [PubMed: 29626364]
11. Wang YF et al. , Overexpression of keratin 17 is associated with poor prognosis in epithelial ovarian cancer. Tumour Biol 34, 1685–1689 (2013). [PubMed: 23430585]
12. Hobbs RP, Batazzi AS, Han MC, Coulombe PA, Loss of Keratin 17 induces tissue-specific cytokine polarization and cellular differentiation in HPV16-driven cervical tumorigenesis in vivo. Oncogene 35, 5653–5662 (2016). [PubMed: 27065324]
13. Wang W, Uberoi A, Spurgeon M, Gronski E, Majerciak V, Lobanov A, Hayes M, Loke A, Zheng ZM, Lambert PF, Stress keratin 17 enhances papillomavirus infection-induced disease by downregulating T cell recruitment. PLoS Pathog 16, (2020).
14. Kim H et al. , Clinical outcomes of immune checkpoint inhibitors for patients with recurrent or metastatic head and neck cancer: real-world data in Korea. BMC Cancer 20, 727 (2020). [PubMed: 32758163]
15. Tumeh PC, Harview CL, Yearley JH, Shintaku IP, Taylor EJM, Robert L, Chmielowski B, Spasic M, Henry G, Ciobanu V, West AN Carmona M, Kivork C, Seja E, Cherry G, Gutierrez A, Grogan TR, Mateus C, Tomasic G, Glaspy JA, Emerson RO, Robins H, Pierce RH, Elashoff DA, Robert C, Ribas A, PD-1 blockade induces responses by inhibiting adaptive immune resistance. Nature, (2014).
16. Judd NP et al. , ERK1/2 regulation of CD44 modulates oral cancer aggressiveness. Cancer Res 72, 365–374 (2012). [PubMed: 22086849]
17. Judd NP, Allen CT, Winkler AE, Uppaluri R, Comparative analysis of tumor-infiltrating lymphocytes in a syngeneic mouse model of oral cancer. Otolaryngol Head Neck Surg 147, 493–500 (2012). [PubMed: 22434099]
18. Zolkind P et al. , Cancer immunogenomic approach to neoantigen discovery in a checkpoint blockade responsive murine model of oral cavity squamous cell carcinoma. Oncotarget 9, 4109–4119 (2018). [PubMed: 29423108]
19. Wingett SW, Andrews S, FastQ Screen: A tool for multi-genome mapping and quality control. F1000Res 7, 1338 (2018). [PubMed: 30254741]
20. Liao Y, Smyth GK, Shi W, The Subread aligner: fast, accurate and scalable read mapping by seed-and-vote. Nucleic Acids Res 41, e108 (2013). [PubMed: 23558742]
21. Liao Y, Smyth GK, Shi W, featureCounts: an efficient general purpose program for assigning sequence reads to genomic features. Bioinformatics 30, 923–930 (2014). [PubMed: 24227677]
22. Law CW, Chen Y, Shi W, Smyth GK, voom: Precision weights unlock linear model analysis tools for RNA-seq read counts. Genome Biol 15, R29 (2014). [PubMed: 24485249]
23. Robinson MD, McCarthy DJ, Smyth GK, edgeR: a Bioconductor package for differential expression analysis of digital gene expression data. Bioinformatics 26, 139–140 (2010). [PubMed: 19910308]
24. Gu Z, Eils R, Schlesner M, Complex heatmaps reveal patterns and correlations in multidimensional genomic data. Bioinformatics 32, 2847–2849 (2016). [PubMed: 27207943]
25. McGinnis CS, Murrow LM, Gartner ZJ, DoubletFinder: Doublet Detection in Single-Cell RNA Sequencing Data Using Artificial Nearest Neighbors. Cell Syst 8, 329–337 e324 (2019). [PubMed: 30954475]
26. Korsunsky I et al. , Fast, sensitive and accurate integration of single-cell data with Harmony. Nat Methods 16, 1289–1296 (2019). [PubMed: 31740819]
27. Stuart T et al. , Comprehensive Integration of Single-Cell Data. Cell 177, 1888–1902 e1821 (2019). [PubMed: 31178118]

28. Finak G et al. , MAST: a flexible statistical framework for assessing transcriptional changes and characterizing heterogeneity in single-cell RNA sequencing data. Genome Biol 16, 278 (2015). [PubMed: 26653891]
29. Efremova M, Vento-Tormo M, Teichmann SA, Vento-Tormo R, CellPhoneDB: inferring cell-cell communication from combined expression of multi-subunit ligand-receptor complexes. Nat Protoc 15, 1484–1506 (2020). [PubMed: 32103204]
30. Aibar S et al. , SCENIC: single-cell regulatory network inference and clustering. Nat Methods 14, 1083–1086 (2017). [PubMed: 28991892]
31. Subramanian A et al. , Gene set enrichment analysis: a knowledge-based approach for interpreting genome-wide expression profiles. Proc Natl Acad Sci U S A 102, 15545–15550 (2005). [PubMed: 16199517]
32. Gordon SM et al. , The transcription factors T-bet and Eomes control key checkpoints of natural killer cell maturation. Immunity 36, 55–67 (2012). [PubMed: 22261438]
33. Bai JDK et al. , Keratin 17 is a negative prognostic biomarker in high-grade endometrial carcinomas. Hum Pathol 94, 40–50 (2019). [PubMed: 31655172]
34. Roa-Pena L et al. , Keratin 17 identifies the most lethal molecular subtype of pancreatic cancer. Sci Rep 9, 11239 (2019). [PubMed: 31375762]
35. Zeng Y et al. , Keratin 17 Suppresses Cell Proliferation and Epithelial-Mesenchymal Transition in Pancreatic Cancer. Front Med (Lausanne) 7, 572494 (2020). [PubMed: 33324659]
36. Ryan MTG Kawalerski R, Roa-Peña Lucia, Leiton Cindy V., Pan Chun-Hao, Torre-Healy Luke A., Boyle Taryn, Snider Natasha T., Shroyer Kenneth R. and Escobar-Hoyos Luisa F., Abstract PO-050: Solubilization of keratin 17 promotes the metastatic dissemination of the most lethal form of pancreatic cancer. Cancer Research, (2020).
37. Grossman JE, Vasudevan D, Joyce CE, Hildago M, Is PD-L1 a consistent biomarker for anti-PD-1 therapy? The model of balstilimab in a virally-driven tumor. Oncogene 40, 1393–1395 (2021). [PubMed: 33500548]
38. Mehra R et al. , Efficacy and safety of pembrolizumab in recurrent/metastatic head and neck squamous cell carcinoma: pooled analyses after long-term follow-up in KEYNOTE-012. Br J Cancer 119, 153–159 (2018). [PubMed: 29955135]
39. Naumann RW et al. , Safety and Efficacy of Nivolumab Monotherapy in Recurrent or Metastatic Cervical, Vaginal, or Vulvar Carcinoma: Results From the Phase I/II CheckMate 358 Trial. J Clin Oncol 37, 2825–2834 (2019). [PubMed: 31487218]
40. Crosta S et al. , PD-L1 Testing and Squamous Cell Carcinoma of the Head and Neck: A Multicenter Study on the Diagnostic Reproducibility of Different Protocols. Cancers (Basel) 13, (2021).
41. Bassez A et al. , A single-cell map of intratumoral changes during anti-PD1 treatment of patients with breast cancer. Nat Med 27, 820–832 (2021). [PubMed: 33958794]
42. Moore E et al. , Established T Cell-Inflamed Tumors Rejected after Adaptive Resistance Was Reversed by Combination STING Activation and PD-1 Pathway Blockade. Cancer Immunol Res 4, 1061–1071 (2016). [PubMed: 27821498]
43. Onken MD et al. , A surprising cross-species conservation in the genomic landscape of mouse and human oral cancer identifies a transcriptional signature predicting metastatic disease. Clin Cancer Res 20, 2873–2884 (2014). [PubMed: 24668645]
44. Chung BM et al. , Regulation of C-X-C chemokine gene expression by keratin 17 and hnRNP K in skin tumor keratinocytes. J Cell Biol 208, 613–627 (2015). [PubMed: 25713416]
45. House IG et al. , Macrophage-Derived CXCL9 and CXCL10 Are Required for Antitumor Immune Responses Following Immune Checkpoint Blockade. Clin Cancer Res 26, 487–504 (2020). [PubMed: 31636098]
46. Dangaj D et al. , Cooperation between Constitutive and Inducible Chemokines Enables T Cell Engraftment and Immune Attack in Solid Tumors. Cancer Cell 35, 885–900 e810 (2019). [PubMed: 31185212]
47. Litchfield K et al. , Meta-analysis of tumor- and T cell-intrinsic mechanisms of sensitization to checkpoint inhibition. Cell 184, 596–614 e514 (2021). [PubMed: 33508232]

48. Cristescu R et al. , Pan-tumor genomic biomarkers for PD-1 checkpoint blockade-based immunotherapy. Science 362, (2018).

49. Zhang M et al. , CCL7 recruits cDC1 to promote antitumor immunity and facilitate checkpoint immunotherapy to non-small cell lung cancer. Nat Commun 11, 6119 (2020). [PubMed: 33257678]

50. Huang B et al. , CCL2/CCR2 pathway mediates recruitment of myeloid suppressor cells to cancers. Cancer Lett 252, 86–92 (2007). [PubMed: 17257744]

51. Qian BZ et al. , CCL2 recruits inflammatory monocytes to facilitate breast-tumour metastasis. Nature 475, 222–225 (2011). [PubMed: 21654748]

52. Seo H et al. , BATF and IRF4 cooperate to counter exhaustion in tumor-infiltrating CAR T cells. Nat Immunol 22, 983–995 (2021). [PubMed: 34282330]

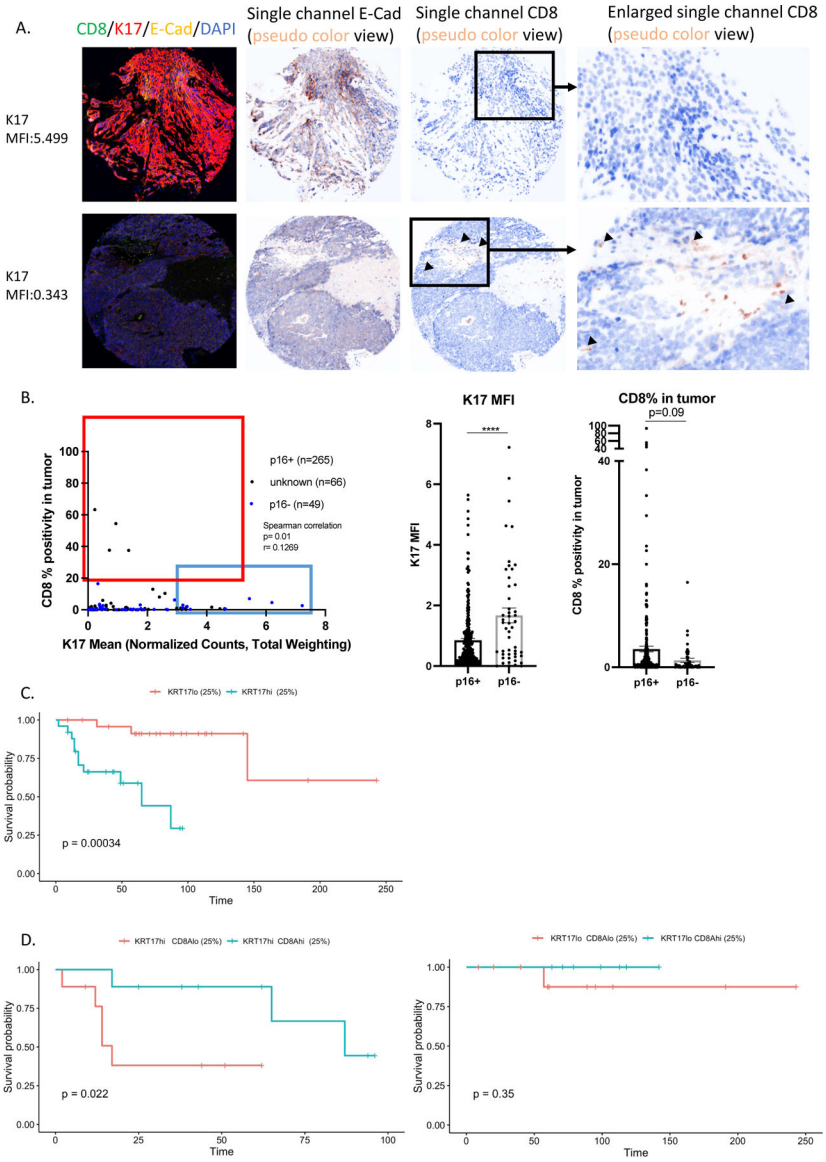

Figure 1. Human head and neck cancer samples with high K17 expression present low level of CD8+ cell infiltration in tumors.

A) Examples of TMA images analyzed for K17 expression level and CD8 % positivity in tumors (E-Cad+). Left column shows fluorescent views of one K17 high tissue and one K17 low tissue, with K17 staining shown in red. Right column shows single color view of E-Cad staining and CD8 staining (orange pseudo color) of the same tissues shown on left side. Far right column shows enlarged image of CD8 staining. **B)** (left) K17 mean fluorescence intensity (X-axis) and CD8 % positivity (Y-axis) in E-cadherin marked tumor regions. Spearman correlation was used. (middle) K17 MFI in p16+ versus p16- samples. Student t-test was used (****p<0.001). (right) %CD8 positivity in tumor for p16+ versus p16- samples. Student t-test was used. **C**) K17 MFI of triplicate primary cancer samples are averaged for the same patient. Log rank test was used to compare survival times between patients in the top 25% K17 MFI range and patients in the bottom 25% K17 MFI range. **D**) Log rank test was used to compare (left) patients that had the most 25% K17 MFI and most

25% CD8 positivity versus patients that had the most 25% K17 MFI and least 25% CD8 positivity; (right) patients that had the least 25% K17 MFI and most 25% CD8 positivity versus patients that had the least 25% K17 MFI and the least 25% CD8 positivity.

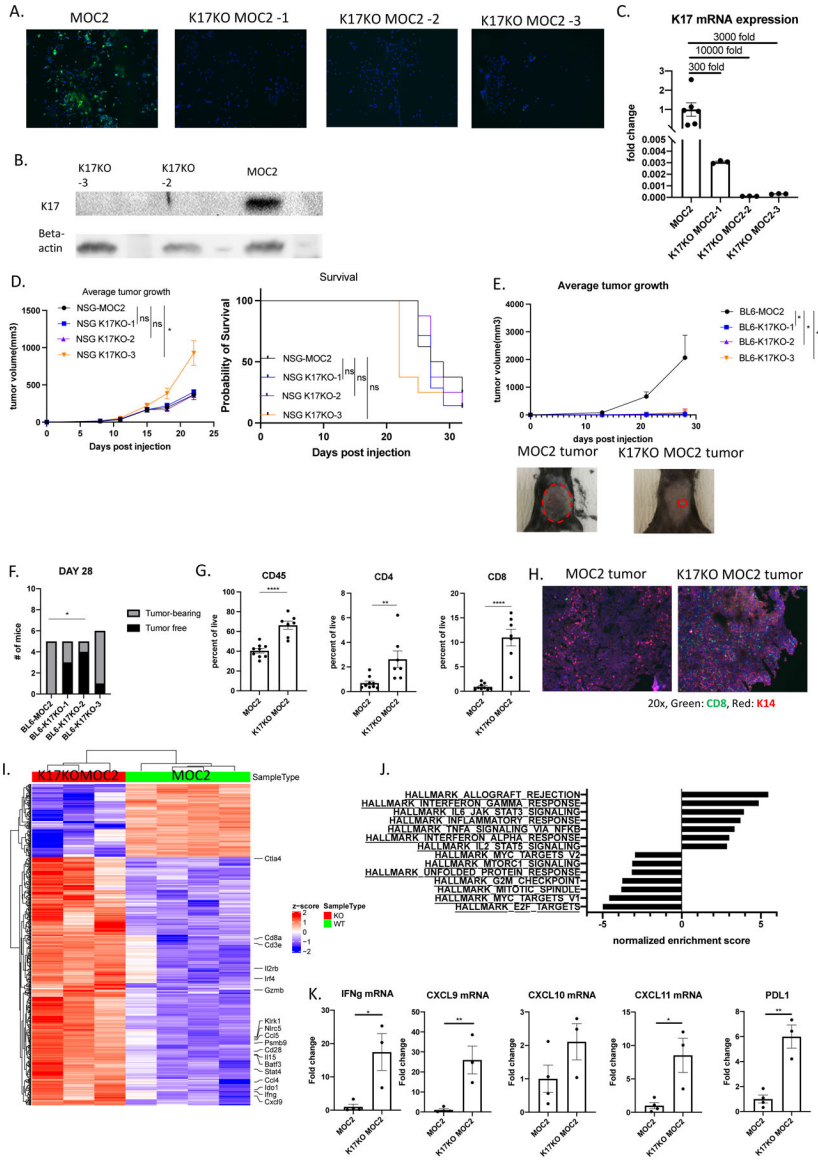

Figure 2. Stress keratin 17 supports syngeneic head and neck cancer cell growth in immunocompetent mice.

A) Immunofluorescent staining of *in vitro* cultured MOC2 cells and 3 K17-KO variants (10x). Green: K17; Blue: DAPI. MOC2: parental MOC2 cells; K17KO MOC2–1: K17KO MOC2 cells CRISPER/Cas9-deleted with gRNA targeting Exon1 of K17 selected in puromycin; K17KO MOC2–2: K17KO MOC2 cells CRISPER/Cas9-deleted with gRNA targeting Exon4 of K17 selected in puromycin; K17KO MOC2–3: K17KO MOC2 cells CRISPER/Cas9-deleted with gRNA targeting Exon5 of K17 selected in puromycin. **B**) Western blot of K17 and beta-actin in proteins collected from MOC2, K17KO-2 and K17KO-3 cell lines. **C**) Relative expression of K17 mRNA measured by qRT-PCR in K17KO MOC2 cell lines *in vitro*, normalized to GAPDH mRNA level in the parental MOC2 cells. Standard errors are shown. **D**) NSG mice were subcutaneously injected with 3×10^5 MOC2 parental cells (n=8 NSG-MOC2), or K17KO MOC2–1 cells (n=7 NSG-K17KO-1), or K17KO MOC2–2 cells (n=8 NSG-K17KO-2), or K17KO MOC2–3 cells

(n=8 NSG-K17KO-3). Tumor sizes were monitored twice weekly. Two-way ANOVA was used to compare tumor size between MOC2 and K17KO MOC2 tumors for each time point;*p<0.05, ns=not significant for any time point (top); Mouse death were recorded or mice were euthanized when tumor reached 15mm in diameter. Log rank was used to compare survival times between groups. **E**) C57BL/6 mice were subcutaneously injected with 3×10^5 MOC2 parental cells (n=5 BL6-MOC2), or K17KO MOC2–1 cells (n=5 BL6-K17KO-1), or K17KO MOC2–2 cells (n=5 BL6-K17KO-2), or K17KO MOC2–3 cells (n=6 BL6-K17KO-3). Tumor sizes were monitored until day 28 post injection. Two-way ANOVA was used to compare tumor size between MOC2 and K17KO MOC2 tumors for each time point; *p<0.05 for day 28 tumor size (top); Representative images of visible tumors from MOC2 tumor and remaining K17KO MOC2 tumor on day 28 post injection (bottom). **F**) Number of mice that completely rejected tumors in C57BL/6 on day 28 post injection. Fisher's exact test was used to compare MOC2 tumor and K17KO MOC2 tumor rejections; *p<0.05. **G**) C57BL/6 mice were subcutaneously injected with 2×10^5 MOC2 parental cells or K17KO MOC2–1 cells or K17KO MOC2–2 cells. Tumors were collected between day 28 to day 31 post injection for flow cytometry of tumor infiltrating CD45, CD4 and CD8 cells. The frequency of CD45, CD4 and CD8 in total live cells were pooled for K17KO MOC2–1 and K17KO MOC2–2 tumors (K17KO MOC2). The data were pooled from two independent repeat experiments. Unpaired t-test was used to compare frequencies in MOC2 tumors versus K17KO MOC2 tumors; **p<0.01, ****p<0.0001. Standard errors are shown. **H**) Immunofluorescent staining of CD8 (green), K14 (red, keratinocyte/tumor cell marker) and DAPI (blue) in MOC2 tumor versus K17KO MOC2 tumor (20x). **I**) Heatmap of differentially expressed genes between K17KO MOC2 tumors versus MOC2 tumors. **J**) Normalized enrichment score of top seven upregulated and top seven downregulated hallmark signaling pathways comparing K17KO MOC2 tumors versus MOC2 tumors, using GSEA analysis. **K**) Relative mRNA expression of IFN**γ**, CXCL9, CXCL10, CXCL11 and PD-L1 in K17KO MOC2 tumors compared to MOC2 tumors, normalized to GAPDH mRNA level, measured by qRT-PCR of bulk tumor RNA.

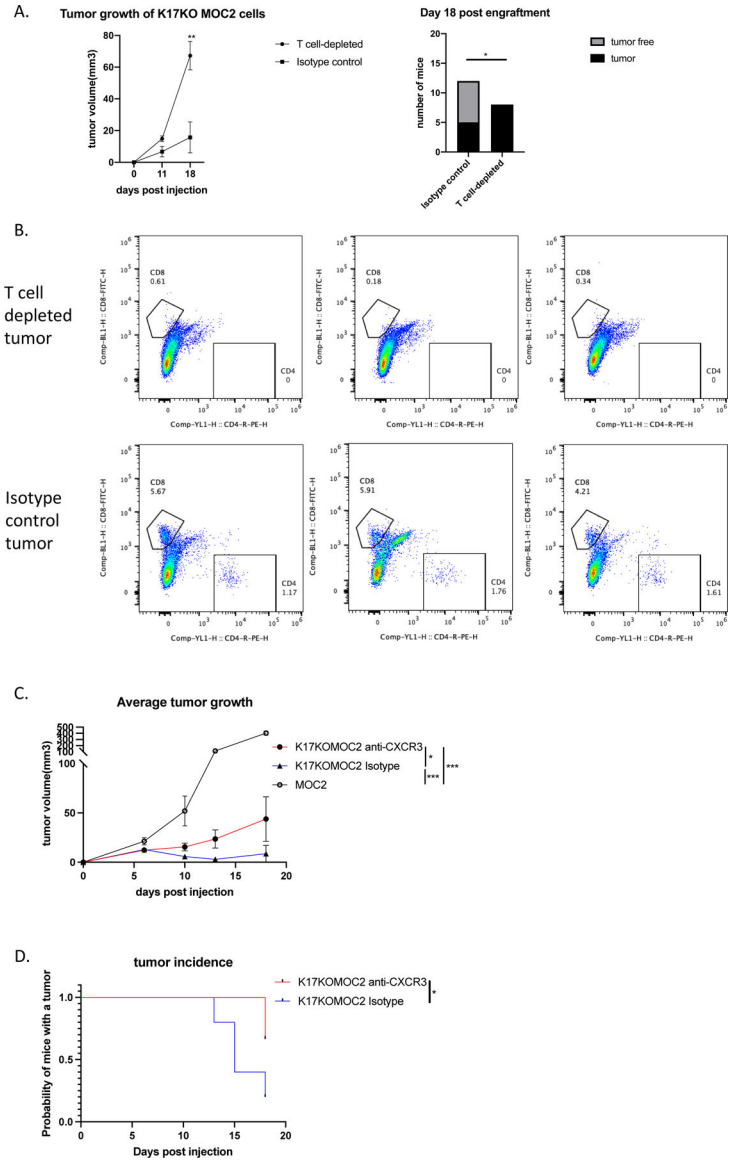

Figure 3. T cells are required for rejection of K17KO MOC2 tumors in C56BL/6 mice.

A) C57BL/6 mice were subcutaneously injected with 2×10^5 K17KO MOC2–2 cells. Mice were depleted for CD4 and CD8 cells starting three days post injection, throughout the study. Tumor sizes were measured on day 11 and day 18 post injection. Left: Two-way ANOVA was used to compare average tumor size at each time point, **p<0.01, standard error is shown. Right: Fisher's exact test was used to compare between two groups for number of mice that completely reject tumor (tumor-free) and number of mice that did not reject tumor (tumor). **B**) Three K17KO MOC2–2 tumors from T cell depleted mice or isotype control mice were collected on day 18 post injection for flow cytometry analysis of tumor-infiltrating CD4 and CD8 cells. Both CD4 and CD8 cells were confirmed depleted from tumors growing in T cell-depleted mice. **C**) A single cell clone of K17KO MOC2–3 cells (K17KOMOC2) or parental MOC2 were injected subcutaneously at 2×10^5 cells into C57BL/6 mice. Mice bearing K17KOMOC2 tumors received anti-CXCR3 or isotype control

antibody starting one day before tumor injection, throughout the study. Tumor sizes were monitored twice every week. Two-way ANOVA was used to compare average tumor size for each time. *p<0.05 for day 18 time point. ***p<0.001 for day 18 time point. Standard errors are shown. **D**) Probability of mice with tumors that persisted (failed to completely regress) in anti-CXCR3 treated mice versus isotype control mice. Gehan-Breslow-Wilcoxon test was used to compare the regression line between two groups. *p<0.05.

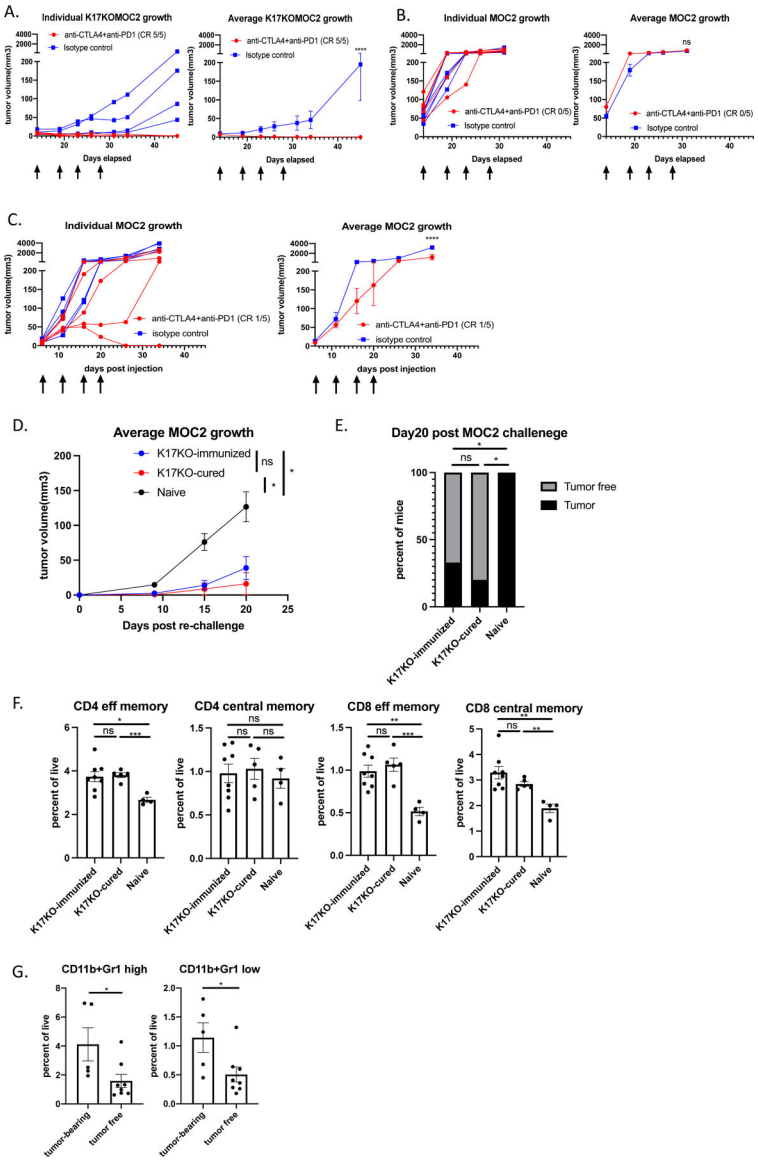

Figure 4. Stress keratin 17 knockout tumors have improved response to immune checkpoint blockade therapy.

C57BL/6 mice were injected with 3×10^5 K17KO MOC2–2 cells or parental MOC2 cells. Mice bearing a K17KO MOC2 tumor that was larger than 2mmx2mm on day 14 post injection and mice bearing MOC2 tumors were subject to anti-CTLA4+anti-PD1 treatment starting on day 14 post injection, for up to four doses (indicated by arrows). Tumor sizes were monitored. CR: complete responder were mice that completely rejected the tumor by day 45 post injection. **A)** Individual (on left) and average (on right) K17KOMOC2 tumor growth are shown. **B**) Individual and average MOC2 tumor growth treated at the same time. **C**) Individual and average MOC2 tumor growth treated at the same size (starting at day 6 post injection for the MOC2 tumors) as the > 2×2 day14-K17KOMOC2 tumors in Figure 4A. Two-way ANOVA was used to compare average tumor size between groups for each time point measured. ns: not significant, ****p<0.0001. **D**) Mice that spontaneously rejected K17KO MOC2 tumors (K17KO-immunized) and mice that completely rejected K17KO

MOC2 tumors upon ICB therapy (K17KO-cured) were subcutaneously re-challenged with 150,000 MOC2 parental cells, along with some naïve control mice. Average MOC2 tumor growth is shown. Two-way ANOVA was used to compare average tumor size between groups for each time point measured. ns: not significant, *p<0.05 for day 20. Standard errors are shown. **E**) Percent of mice that were able to reject MOC2 tumors (tumor-free) and percent of mice that did not reject MOC2 tumors (tumor). Fisher's exact test used to compare between each group. ns: not significant, *p<0.05. **F**) Spleens from all mice in Figure 4D were collected on day 20 post MOC2 injection. Spleen cells were subject to flow cytometry analyses for effector memory (eff memory) and central memory defined by CD44 and CD62L staining. One-way ANOVA was used to compare the frequency of memory cells in total live spleen cells between each group. ns: not significant, *p<0.05, **p<0.01, ***p<0.001. **G**) Spleen cells from K17KO-immunized mice and K17KO-cured mice that were challenged with MOC2 cells in Figure 4D were subject to CD11b and Gr1 analyses by flow cytometry. Student t-test was used to compare cell frequency between mice that rejected MOC2 tumors (tumor free) versus mice that did not reject MOC2 tumors (tumor-bearing).*p<0.05.

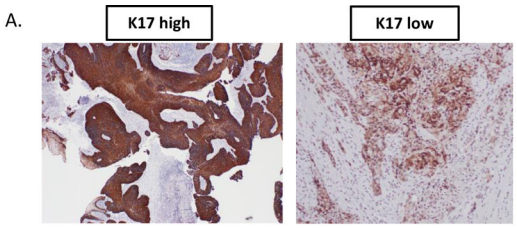

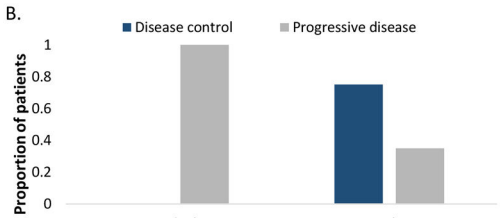

	K17 high		K17 low		Total	
Response status						
Disease control	0	(0.0%)	6	(75.0%)	6	(23.1%)
Progressive disease	18	(100.0%)	2	(25.0%)	20	(76.9%)
p value (Fisher's exact test)		**0.001**				

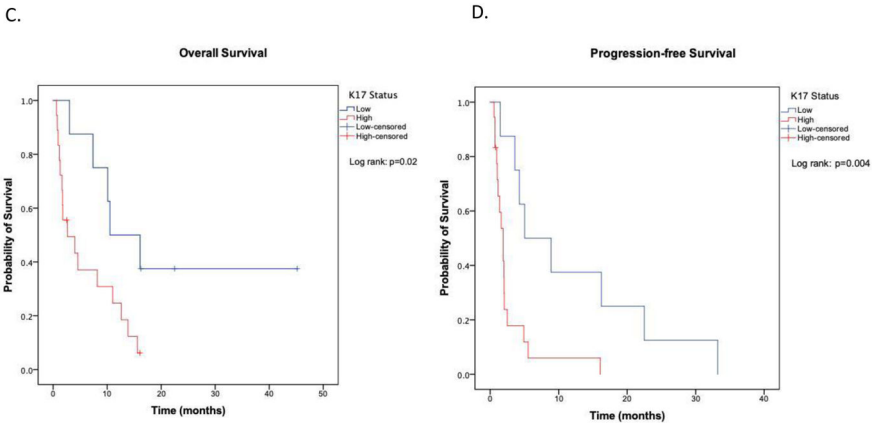

Figure 5. High level of K17 expression in head and neck cancer is associated with poor response to anti-PD1 immunotherapy.

A) Two representative images for K17 high and K17 low tissue (20x). **B**) Association analysis between pretreatment tumor K17 expression and clinical response was based on a high expression cut-off of >5% strong cytoplasmic staining in tumor cells. Fisher's exact test was used. **C**) Kaplan-Meier estimates of overall survival. Log rank test was used. **D**) Kaplan-Meier estimates of progression-free survival (PFS). Log rank test was used.

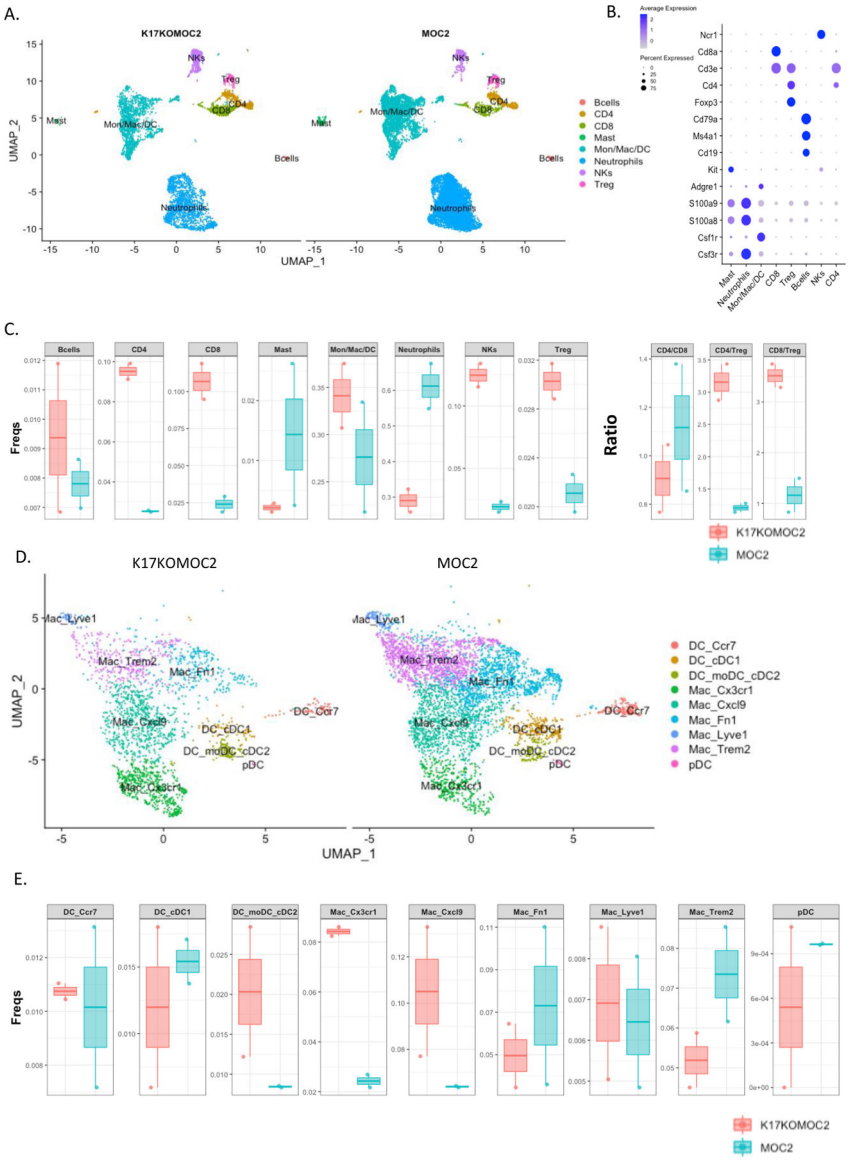

Figure 6. K17KO MOC2 tumors had switched tumor immune microenvironment phenotypes.

A) UMAP (Uniform Manifold Approximation and Projection) high-dimensional deductional map of 21,894 CD45+ cells between MOC2 and K17KOMOC2 tumors (2 replicates each group) and the annotation of major immune cell-types: T cells (CD4/CD8/Treg), NKs, Mast cells, B cells, Neutrophils, Monocytes/Macrophages/DCs. **B**) Representative markers' expression of major immune cell-types, color presented scaled average expression levels, circle size presents the percentage of cells that expressed specific markers. **C**) Frequencies of major immune-cell types (out of CD45+ cells) and the ratio of CD4/CD8, CD4/Treg, CD8/Treg between K17KOMOC2 and MOC2 tumors. **D**) UMAP of 6,737 myeloid cells (excluding neutrophils) including different DCs and Macrophage subsets; the macrophage subset were named using the representative marker in each subset (Supplementary Figure 9).

E) Frequencies of 9 DC and macrophage subsets (out of number of CD45+ cells) between K17KO vs MOC2.